

See discussions, stats, and author profiles for this publication at: <https://www.researchgate.net/publication/42438234>

# Monitoring Scanning Electrochemical Microscopy Approach Curves with Mid-Infrared Spectroscopy: Toward a Novel Current-Independent Positioning Mode

ARTICLE in ANALYTICAL CHEMISTRY · MARCH 2010

Impact Factor: 5.64 · DOI: 10.1021/ac902781h · Source: PubMed

---

CITATIONS

8

---

READS

31

## 3 AUTHORS:



Liquun Wang

Tokyo Denki University

75 PUBLICATIONS 1,085 CITATIONS

SEE PROFILE



Christine Kranz

Universität Ulm

130 PUBLICATIONS 2,448 CITATIONS

SEE PROFILE



Boris Mizaikoff

Universität Ulm

310 PUBLICATIONS 4,799 CITATIONS

SEE PROFILE

Published in final edited form as:

*Anal Chem.* 2010 April 15; 82(8): 3132–3138. doi:10.1021/ac902781h.

# Monitoring Scanning Electrochemical Microscopy Approach Curves with Mid-Infrared Spectroscopy – Towards a Novel Current-Independent Positioning Mode

Liqun Wang<sup>1</sup>, Christine Kranz<sup>2</sup>, and Boris Mizaikoff<sup>2,\*</sup>

<sup>1</sup>School of Chemistry and Biochemistry, Georgia Institute of Technology, Atlanta, GA 30332

<sup>2</sup>Institute of Analytical and Bioanalytical Chemistry, University of Ulm, Ulm, GER

## Abstract

Single-bounce attenuated total reflection infrared spectroscopy in the 3–20  $\mu\text{m}$  range (MIR) has been combined with scanning electrochemical microscopy (SECM) for *in situ* spectroscopic detection of electrochemically induced localized surface modifications using an ultramicroelectrode (UME). In this study, a novel current-independent approach for positioning the UME in aqueous electrolyte solution is presented using either changes of IR absorption intensity associated with borosilicate glass (BSG), which is used as shielding material of the UME wire, or by monitoring IR changes of the water spectrum within the penetration depth of the evanescent field due to displacement of water molecules in the volume between the sample surface and the UME within the evanescent field. The experimental results show that the UME penetrates into the exponentially decaying evanescent field in close vicinity (a few  $\mu\text{m}$ ) to the ATR crystal surface. Hence, the resulting intensity changes of the IR absorption spectra for borosilicate glass (increase) and for water (decrease), can be used to determine the position of the UME relative to the ATR crystal surface independent of the current measured at the UME.

## Introduction

In recent years, scanning electrochemical microscopy (SECM) has ventured into a diverse field of applications providing information on homogeneous and heterogeneous electron transfer mechanism at a variety of solid/liquid, liquid/liquid and air/liquid interfaces.<sup>2, 3</sup> In addition, SECM has been successfully used for microstructured surface modifications using deposition or etching processes.<sup>4</sup> Furthermore, SECM has been combined with a variety of analytical techniques ranging from mass sensitive and optical analyses to complementary scanning probe techniques providing in addition structural and time-resolved information on interface processes. For example, electrochemical quartz crystal microbalance (EQCM)-SECM<sup>5–10</sup>, electrochemical scanning tunneling microscopy (ESTM)-SECM,<sup>11, 12</sup> photoelectrochemical (PEM)-SECM,<sup>13</sup> and AFM-SECM<sup>14–20</sup> have been realized. SECM has also been combined with optical microscopy,<sup>21, 22</sup> near-field scanning optical microscopy (NSOM),<sup>23, 24</sup> fluorescence spectroscopy,<sup>25</sup> chemiluminescence,<sup>26–29</sup> and surface plasmon resonance (SPR).<sup>30</sup> Most recently, a novel combination of SECM with spectroscopic techniques in the mid-infrared regime of the electromagnetic spectrum has been developed by our research group.<sup>1</sup> This combination allows simultaneously investigating *in situ* electrochemically induced processes *via* single-bounce attenuated total reflection infrared spectroscopy (IR-

\*Corresponding author. boris.mizaikoff@uni-ulm.de.

ATR). Furthermore and as shown here, the combination IR-ATR-SECM enables a novel current-independent positioning mode for the ultramicroelectrode (UME).

In conventional SECM experiments, the positioning of the UME is achieved by monitoring the faradaic current measured at the UME when approaching the sample surface. Several mathematical models - depending on the UME geometry and the electroconductivity of the sample surface - were developed, and are well established to determine the distance of the tip to the sample surface derived from the feedback current measured at the microelectrode.<sup>31–39</sup> However, determining the UME-to-sample distance based on the resulting approach curves is limited to amperometric experiments, and requires UMEs with well-defined tip geometries. In addition, the faradaic current may be affected not only by the electroconductivity of the sample surface, but also by the sample morphology, as the UME is usually kept at a constant height during SECM imaging at a distance of a couple of electrode radii (with typical radii of UMEs used in conventional SECM experiments in the range of 2.5 – 12.5  $\mu\text{m}$ ). Hence, non-amperometric positioning modes are of substantial interest for separating the current from the distance information, and are the subject of continuous research. For example, non-amperometric UME positioning was achieved by measurement of the solvent resistance, when the UME tip is close to the sample surface.<sup>40, 41</sup> Shear-force based UME positioning optically<sup>42</sup> or non-optically<sup>43–45</sup> detects changes of shear-forces once the tip is in close proximity to the sample surface. This positioning mode has been adapted from near field scanning optical microscopy, and is among the most commonly used non-amperometric techniques for controlling the distance between tip and sample surface. Most recently, the combination AFM-SECM has been developed enabling control on the distance between a submicro- or nanosized electrode and the sample surface based on the well-established force detection in AFM.<sup>14–20</sup> The combination of IR-ATR-SECM has the potential to provide an alternative positioning mode for controlling the distance between the UME and the sample surface independent from the electrochemical signal. A schematic representation of the IR-ATR-SECM setup is shown in Fig. 1. IR-ATR is an attractive spectroscopic technique due to its exquisite and highly localized surface sensitivity.<sup>46</sup> Probably the most relevant advantage of IR-ATR is the fact that strong IR absorbers, such as water, show less pronounced spectral interferences in IR-ATR absorption measurements compared to conventional transmission and reflection mode IR spectroscopy due to the limited probed volume defined by the penetration depth of the evanescent field. IR radiation coupled into an internal reflection element at angles exceeding the critical angle propagates along this waveguide. Given a refractive index  $n_1$  of the waveguide, and  $n_2$  of the surrounding medium (with  $n_1 > n_2$ ), an evanescent field is formed penetrating a short distance beyond the interface into the optically rare medium. The intensity of the evanescent field exponentially decays with distance to the interface; the penetration depth is typically in the range of a few micrometers in the MIR spectral regime. The penetration depth depends on the wavelength of the radiation, the refractive indices of the waveguide material and the ambient medium, and on the angle of incidence.<sup>46</sup> Hence, IR absorbing molecules present in close vicinity to the waveguide surface may interact with photons similar to transmission absorption experiments, thereby providing evanescent field absorption spectra.<sup>46</sup> If an UME is approaching the ATR waveguide surface and penetrates the evanescent field, the sheath material of the UME - usually borosilicate glass (BSG) - generates an IR evanescent field absorption spectrum. Borosilicate glass has several strong IR absorption features in the regime 1600-700  $\text{cm}^{-1}$ ,<sup>47, 48</sup> such as the B-O stretching mode at 1380  $\text{cm}^{-1}$ , the Si-O stretching mode at 1130 and 880  $\text{cm}^{-1}$ , and the Si-O bending mode at 760  $\text{cm}^{-1}$ . With a changing distance (or UME volume) within the evanescent field, the IR intensity of BSG features change in correlation to the distance or volume of glass, respectively. In addition, as the volume of the UME within the evanescent field increases, the volume of the aqueous solution in the gap between the sample surface and the UME decreases, which results in correlated changes of the O-H vibrational mode of water at 1640  $\text{cm}^{-1}$ . Hence, intensity changes of spectral features

either of the UME or of the surrounding solution may be correlated with the distance of the UME to the sample surface.

In this study we present a novel concept utilizing IR-ATR absorption signals for determining the tip-sample distance at microelectrodes with a RG value of 10 (RG is  $Rg/a$ , where  $Rg$  is the radius of the insulating glass and  $a$  the radius of the microwire), which are typically used in SECM experiments. Approach curves of UMEs toward IR transparent substrates were studied via IR evanescent field absorption signatures at ambient conditions and in electrolyte solution. Experimentally obtained IR-ATR data were then fitted with a mathematical model enabling correlating the penetration depth at different wavenumbers with the distance to the waveguide surface, and were finally compared to the theoretically calculated values.

## Experimental

### Combined IR-ATR-SECM instrument

A detailed description of the combined IR-ATR-SECM instrument is described elsewhere.<sup>1</sup> In brief, broadband IR radiation from a FT-IR spectrometer (IRCube-M, Bruker Optics Inc., Billerica, MA) is externally collimated and focused onto the curvature of a single-bounce hemispherical ZnSe ATR crystal (3 mm in diameter, Harrick Scientific, Pleasantville, NY) by an off-axis parabolic mirror (OAP). The internally reflected radiation from the top flat surface of the ATR crystal is then collimated by a second OAP, and focused by a third OAP onto a liquid nitrogen cooled mercury-cadmium-telluride (MCT) detector. The ATR crystal is built into an electrochemical cell serving as the central component of the cell base plate, as schematically shown in Fig. 1. The micropositioning system moving the microelectrode above the ATR crystal is part of a homebuilt SECM system driven by stepper motors (Scientific Precision Instruments GmbH®, Oppenheim, Germany) with a precision of 0.02  $\mu\text{m}$ , and correlated with the positioning of the UME using an A/D-D/A board (DAS 1602-16, Plug-In-Electronic, Eichenau, FRG). All electrochemical experiments were conducted with a CHI 842A bipotentiostat (CH Instruments, Inc., Austin, TX). The combined IR-ATR-SECM system was located in a dark box and purged with nitrogen to maintain an inert and stable atmosphere during IR measurements. All IR spectra recorded with the IR-ATR-SECM instrument were collected at a spectral resolution of 4  $\text{cm}^{-1}$  averaging 64 scans. The recorded spectra were analyzed using the OPUS software package (Bruker, Optics Inc., Billerica, MA).

### UME preparation

Disk-shaped microelectrodes were fabricated as previously described<sup>4</sup> by sealing a 25  $\mu\text{m}$  (diam.) Pt wires under vacuum into borosilicate glass capillaries. Successive grinding with diamond paste (6  $\mu\text{m}$  and 3  $\mu\text{m}$ ), and polishing with alumina paste (1  $\mu\text{m}$  and 0.05  $\mu\text{m}$ ), respectively, exposes disk-shaped microelectrodes. Characterization of the UME was performed by cyclic voltammetry.

### Chemicals

$\text{Ru}(\text{bpy})_3\text{Cl}_2 \cdot 6\text{H}_2\text{O}$  and KCl (Reagent grade) were obtained from Sigma Aldrich (St. Louis, MO). 0.02 M  $\text{Ru}(\text{bpy})_3\text{Cl}_2/0.1$  M KCl electrolyte solution was prepared in deionized  $\text{H}_2\text{O}$  (Milli-Q water system, Millipore Corp., Billerica, MA). All solutions were purged with UHP argon (Airgas, Hapeville, GA) prior to electrochemical experiments.

### SECM approach curves

All experiments were performed using a three-electrode configuration entailing a disk-shaped 25  $\mu\text{m}$  (diam.) Pt UME working electrode, a 1 mm (diam.) Pt auxiliary electrode, and an Ag/AgCl quasi reference electrode. The experiments were conducted in a Faraday cage. Faraday

currents were obtained due to the oxidation of  $\text{Ru}(\text{bpy})_3\text{Cl}_2 \cdot 6\text{H}_2\text{O}$  at the UME. These currents were recorded by applying a constant potential of 1.13 V *vs.* Ag/AgCl to the UME during the approach toward the ATR crystal surface at an approach speed of 1.6  $\mu\text{m/s}$  with a data recording interval (i.e. obtaining IR spectra) of 0.4  $\mu\text{m}$ ; within the evanescent field, these intervals were reduced to 0.2  $\mu\text{m}$ .

### Monitoring UME approach curves via IR evanescent field absorption

Experiments were performed both at ambient conditions (air) and in aqueous electrolyte solution containing 0.02 M  $\text{Ru}(\text{bpy})_3\text{Cl}_2/0.1$  M KCl. The 25  $\mu\text{m}$  (diam.) Pt UME was aligned with the center of the ATR crystal using the SECM micropositioning system; then, the UME was approached toward the ATR crystal surface until penetration of the evanescent field was detected via the absorption signal of the UME. UME movement was stopped once the surface of the ATR crystal was reached. During the approach, corresponding series of IR absorption spectra were recorded in air and in electrolyte solution at intervals of 0.4  $\mu\text{m}$  (outside the evanescent field) and 0.2  $\mu\text{m}$  (within the evanescent field), respectively.

### Modeling the UME approach within the evanescent field

A mathematical model of the IR absorption change *vs.* distance between the UME and the surface of the ATR crystal was derived based on the Beer-Lambert law taking into account the exponential decay of the evanescent field intensity. Subsequently, this model was used to fit the experimentally obtained UME approach curves derived from evaluating the absorption changes evident within a series of IR-ATR evanescent field absorption spectra. The values obtained for the penetration depth ( $d_p$ ) derived from this model fitted to the experimentally obtained IR-ATR data were then compared to the calculated values based on the theoretical equation established by Harrick:<sup>46</sup>

$$d_p = \frac{\lambda}{2\pi \sqrt{n_1^2 \sin^2(\theta) - n_2^2}}, \quad (1)$$

where  $\lambda$  is the wavelength of light,  $n_1$  is the refractive index of the ATR waveguide,  $n_2$  is the refractive index of the adjacent medium (with  $n_1 > n_2$ ), and  $\theta$  is the angle of incidence at the interface between waveguide surface and sample.

## Results and discussion

An absorption ( $A$ ) change resulting from the presence of different quantities of an IR-absorbing sample is generally described by the Beer-Lambert law:

$$A = \varepsilon lc = \log \frac{I_0}{I}, \quad (2)$$

where  $\varepsilon$  represents the molar absorptivity of the sample,  $l$  describes the absorption path length (and – as detailed below – the fraction of absorbing material within the evanescent field), and  $c$  gives the concentration of the sample. In addition, the IR absorption is proportional to the ratio of incident light intensity ( $I_0$ ) and the intensity of the radiation after passing through the sample ( $I$ ). However, in case of attenuated total reflection the electromagnetic field ( $E$ ) leaks exponentially decaying into the adjacent medium containing the absorbing sample molecules.<sup>46</sup> Hence, in order to describe the absorption of an analyte within the evanescent field ( $A_{\text{IRATR}}$ ) emanating at the surface of an ATR waveguide this exponential decay has to be taken into account by modifying the Beer-Lambert law (eq. 1) as follows:

$$A_{IRATR} = \frac{E}{E_0} \varepsilon l c, \quad (3)$$

where  $E$  (with  $E_1 \dots E_{n-1}$  indicating the decreasing intensity of the evanescent field) is the intensity of the evanescent field, and  $E_0$  is the (maximum) intensity at the surface of the ATR waveguide. The relationship between  $E$  and  $E_0$  may be expressed by:<sup>46</sup>

$$E = E_0 e^{\left(\frac{-z}{d_p}\right)}, \quad (4)$$

where  $z$  describes the distance from the ATR crystal surface for an exponentially decayed fraction of the initial energy  $E_0$  (indicated in Fig. 2b by green boxes representing different  $E$  values at different positions  $\Delta z$ ). Replacing  $E$  in eq (3) with the expression in eq (4) leads to:

$$A_{IRATR} = e^{\left(\frac{-Z}{d_p}\right)} \varepsilon l c \quad (5)$$

From eq. (5) one can derive that the absorption within the evanescent field is a function of the fraction  $l$  of absorbing material between  $d_{max}$  and  $z$ , and the distance  $z$ . Figure 2a schematically shows the adjacent medium (air or electrolyte solution) represented as a cylinder, into which the absorbing sample – here, the UME with an IR-absorbing borosilicate glass sheath - is penetrating, if the UME approaches toward the ATR crystal surface. This cylinder is defined by a bottom radius ( $r_{ATR}$ ), which is determined by radius of the sensing area of the hemispherical ATR crystal. The height of the cylinder ( $d_{max}$ ) describes the distance from the ATR crystal surface where no IR absorption from the BSG shielding of the UME is detectable anymore, represented as the light gray part of the UME (Note: the evanescent field may penetrate beyond  $d_{max}$  into the adjacent medium, however, given the minute intensity of the evanescent field no IR absorption changes can be detected anymore). If the UME approaches toward the ATR crystal surface and penetrates beyond  $d_{max}$  into the evanescent field, IR absorptions specific to the BSG will change (i.e., increase) with the  $z$ -position of the UME due to the increasing quantity of absorbing material (i.e., “volume of the UME” shown as dark gray part of the UME) present within the evanescent field. In this case,  $z = 0$  means that the electrode is touching the ATR crystal surface (Fig. 2b, left). The obtained absorption signal is convoluted with the exponential increase of the evanescent field intensity toward the ATR waveguide surface. In order to describe thus obtained absorption signals, eq (5) may be formulated taking the fraction of absorbing material between  $d_{max}$  and  $z$  into account as follows:

$$A_{IRATR} = \sum_{i=0}^i e^{-z_i/d_p} \cdot \varepsilon \Delta z_i c = \int_z^{d_{max}} K e^{-z_i/d_p} \cdot dz = K(e^{-z/d_p} - e^{-d_{max}/d_p}) = P e^{-z_i/d_p} - Q, \quad (6)$$

where  $K$ ,  $P$ , and  $Q$  are constants for a given material system, and  $d_{max}$  and  $d_p$  are assumed to be constants that will not change while approaching the UME towards the waveguide surface. This model shows that – as expected - the IR absorption signal exponentially decays with increasing distance  $z$  between the UME and the ATR crystal surface.

Figure 3 (a) shows an example of IR spectra recorded during an UME approaching within the evanescent field in air. The IR features of BSG are evident at different wavenumbers including e.g., the B-O stretching mode at  $1380 \text{ cm}^{-1}$ , the Si-O stretching mode at  $1130$  and  $880 \text{ cm}^{-1}$ , and the Si-O bending mode at  $760 \text{ cm}^{-1}$ .<sup>47, 48</sup> With the UME approaching the ATR surface,



the absorption intensities for these IR absorption features clearly increase, and eventually reach a maximum if the UME is touching the ATR crystal surface (i.e., the last three spectra – orange, blue, green - in Fig. 3 (a)). The last two IR spectra (orange, blue) show entire overlap, which indicates that the UME is in contact with the ATR crystal surface. However, the observed absorptions are slightly larger than evident for the third spectrum (green), which may be attributed to a slight tilting of the UME initiated by the movement imposed from the micropositioner. Two BSG absorptions at  $1380\text{ cm}^{-1}$  and  $976\text{ cm}^{-1}$  were selected for evaluation enabling to establish IR-ATR approach curves, as shown in Fig. 3 (b) and (c). The error bars in Fig. 3 (b) and (c) were calculated based on the results of three consecutive experiments of the UME approaching the waveguide surface in air, and account for the reproducibility of this novel positioning mode. Thus obtained experimental approach curves were then fitted using the mathematical model established in eq. (6) confirming excellent agreement.

Consecutive approach experiments were also performed in  $0.02\text{ M Ru(bpy)}_3\text{Cl}_2/0.1\text{ M KCl}$  electrolyte solution. A representative series of IR spectra for an approach curve recorded in electrolyte solution is displayed in Fig. 4. In contrast to experiments in air, an additional interesting effect is observed. If the UME approaches the ATR crystal surface, a corresponding volume of electrolyte solution is displaced within  $d_{max}$  and replaced with BSG. Hence, while BSG absorption features should increase, absorptions related to water/electrolyte solution should correspondingly decrease.

The IR absorption spectrum displayed in Fig. 4 (a) shows the decrease of the O-H bending mode of water at  $1640\text{ cm}^{-1}$  with decreasing distance between the UME and the ATR crystal surface. The IR absorption spectrum in Fig. 4 (b) displays the IR features associated with the BSG sheath of the UME, which are overlapping with the shoulder of the water libration mode in the spectral range of  $1200\text{--}700\text{ cm}^{-1}$ . However, the B-O stretching vibration at approx.  $1380\text{ cm}^{-1}$  is located in an IR-transparent window of water thus remaining clearly visible, and reveals the expected increase with decreasing distance between UME and ATR crystal.

Correspondingly, the decreasing water absorption at  $1640\text{ cm}^{-1}$  and the increasing BSG absorption at  $1380\text{ cm}^{-1}$  have been used for establishing IR-assisted UME approach curves in solution. A similar approach curve is anticipated evaluating either absorption feature, as the same volume of water was displaced from the analytical volume probed by the evanescent field that was introduced by the UME penetrating into this regime. An IR absorption spectrum of  $0.02\text{ M Ru(bpy)}_3\text{Cl}_2/0.1\text{ M KCl}/\text{H}_2\text{O}$  was recorded as reference spectrum with the UME located outside  $d_{max}$ . The absolute changes of the IR absorbance at  $1640\text{ cm}^{-1}$  (Fig. 4(c)) and  $1380\text{ cm}^{-1}$  (Fig. 4 (d)) approach experiments were evaluated for establishing IR-ATR approach curves at these two frequencies. Both experimental approach curves were fitted with the developed mathematical model given in eq. (6) and again revealed excellent agreement.

In a next step, the values obtained for the penetration depth derived from the model fitted to the IR-ATR experimental data were compared to the values calculated using the theoretical equation for the penetration depth  $d_p$  (eq 1). To simplify the calculations of the penetration depths at the wavenumbers  $1640\text{ cm}^{-1}$ ,  $1380\text{ cm}^{-1}$ , and  $976\text{ cm}^{-1}$ , the refractive indices of pure BSG (1.5), and water (1.3) or air (1.0) were used. The results derived from experimental data and theoretical calculations comply well, and are summarized in Table 1. The results for the penetration depth derived from the model fitted to the experimental data are in between the theoretically calculated penetration depth results using either the refractive index of pure BSG or of pure water representing the rare optical medium for experiments with the UME approaching in electrolyte solution. The same results were obtained for comparing experiment and calculation for the UME approach conducted in air. The differences between the experimentally derived and the theoretically calculated values may be associated with the

simplified assumption using refractive indices of pure rare media, but are certainly within acceptable tolerances for confirming the validity of the developed approach.

Finally, conventionally recorded feedback mode SECM approach curves were correlated with IR-assisted approach curves both recorded in 0.02 M Ru(bpy)<sub>3</sub>Cl<sub>2</sub>/0.1 M KCl electrolyte solution. Figure 5 (a) shows a conventional amperometric SECM approach curve toward a ZnSe substrate recorded in 0.02M Ru(bpy)<sub>3</sub>Cl<sub>2</sub> / 0.1M KCl/H<sub>2</sub>O electrolyte solution. During amperometric SECM experiments, the UME is usually stopped at a position where the Faradic current has dropped by approx. 20–30 % of the bulk current in order to avoid damage of the UME tip and/or sample by touching the surface. At this value, the electrode is approx. 30 μm away from the substrate surface, as indicated by the red arrow in Fig. 5 (b). The correlation of the electrochemical approach curve and the IR-assisted approach curve both recorded with the same UME in the same 0.02 M Ru(bpy)<sub>3</sub>Cl<sub>2</sub>/0.1 M KCl electrolyte solution is shown in Figure 5 (b). While both modes for establishing the UME distance to the sample surface appear to work well, the IR-ATR signal provides the main advantage that it is recorded independent of the measured Faradaic current. Hence, IR-assisted positioning may be implemented in a feedback loop similar to the shear force mode<sup>44</sup>, and hence, the electrode may be positioned at a known constant distance to the sample surface within the evanescent field emanating from the IR waveguide surface.

## Conclusions

In this study, attenuated total reflection infrared spectroscopy (IR-ATR) was successfully applied to monitor the distance of an ultramicroelectrode (UME) to the sample surface within the penetration depth of the evanescent field generated at an IR-transparent substrate. A mathematical model was derived and fitted to the experimentally obtained data revealing excellent agreement, and the penetration depths derived from IR-assisted approach experiments comply well with the theoretically calculated values. In addition, IR-assisted approach curves provide excellent correlation with conventional feedback mode SECM approach curves recorded in electrolyte solution containing a suitable redox mediator. Consequently, IR-assisted approach curves provide a novel current-independent UME positioning method particularly suitable for non-amperometric combined IR-ATR-SECM experiments, thereby enabling precisely positioning an UME within a distance of a few micrometers above the optical waveguide. Hence, the resolution in SECM experiments may be improved by confining the diffusion due to a reduction of the distance between UME tip and substrate given the fidelity of the distance determination via the evanescent field. Finally, for future developments the IR-ATR approach method may prove particularly useful, if mid-infrared transparent thin film electrodes (such as e.g., diamond-like carbon (DLC) films) are coated onto the ATR crystal surface, or if potentiometric sensors or enzyme electrodes are applied as UME.

## Acknowledgments

The authors acknowledge S.- S. Kim for valuable discussions. Financial support by the National Institute of Health, NIH (Grant R01-EB000508) is also greatly acknowledged.

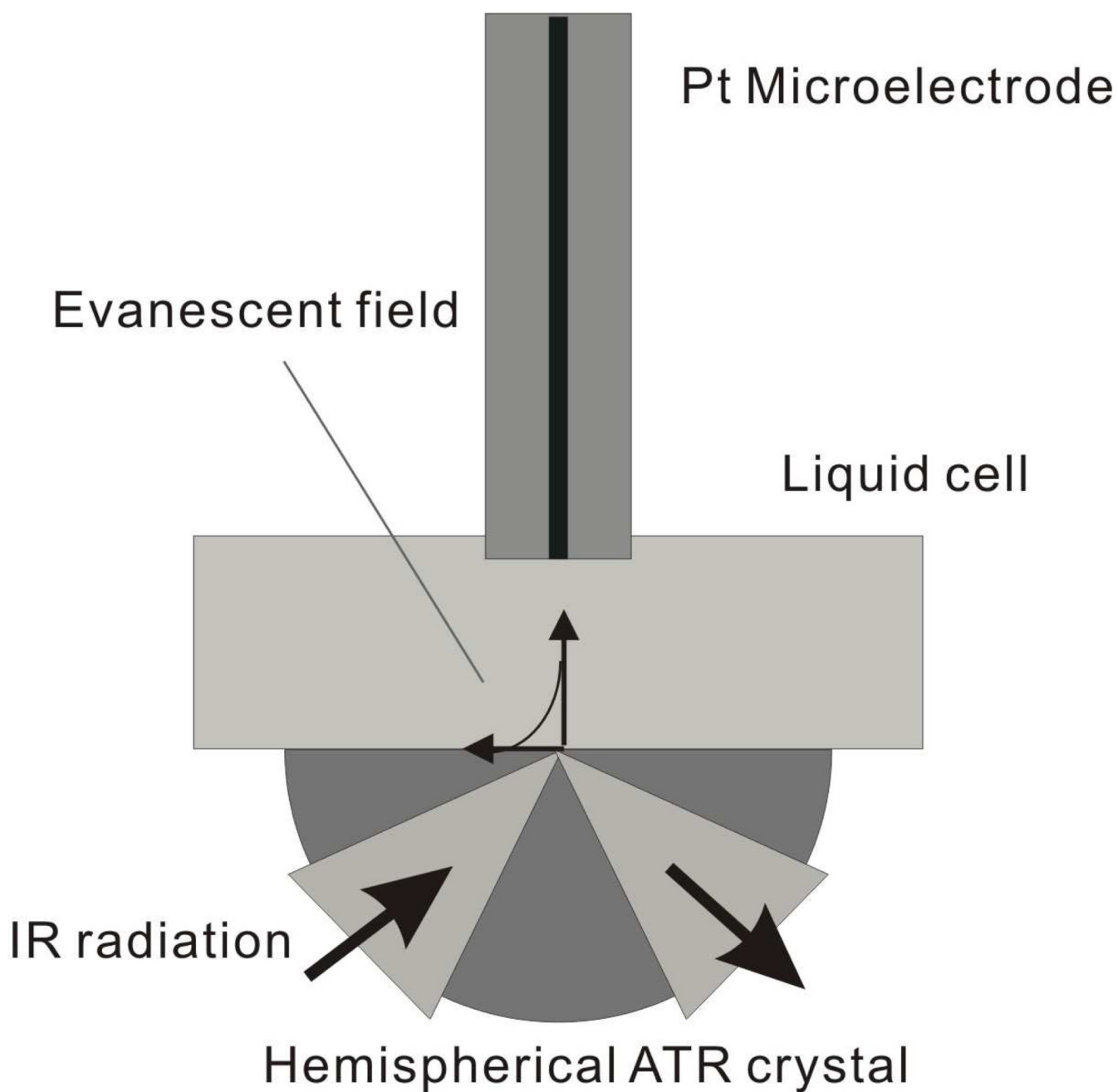
## References

1. Wang L, Kowalik J, Mizaikoff B, Kranz C. Anal. Chem., submitted. 2009
2. Wittstock G, Burchardt M, Pust SE, Shen Y, Zhao C. Angew. Chem. Int. Ed 2007;46:1584–1617.
3. Sun P, Laforge FO, Mirkin MV. Phys. Chem. Chem. Phys 2007;9:802–823. [PubMed: 17287874]
4. Bard, AJ.; Mirkin, MV. Scanning Electrochemical Microscopy. New York: Marcel Dekker; 2001.
5. Shin M, Jeon IC. Bull. Korean Chem. Soc 1998;19:1227–1232.



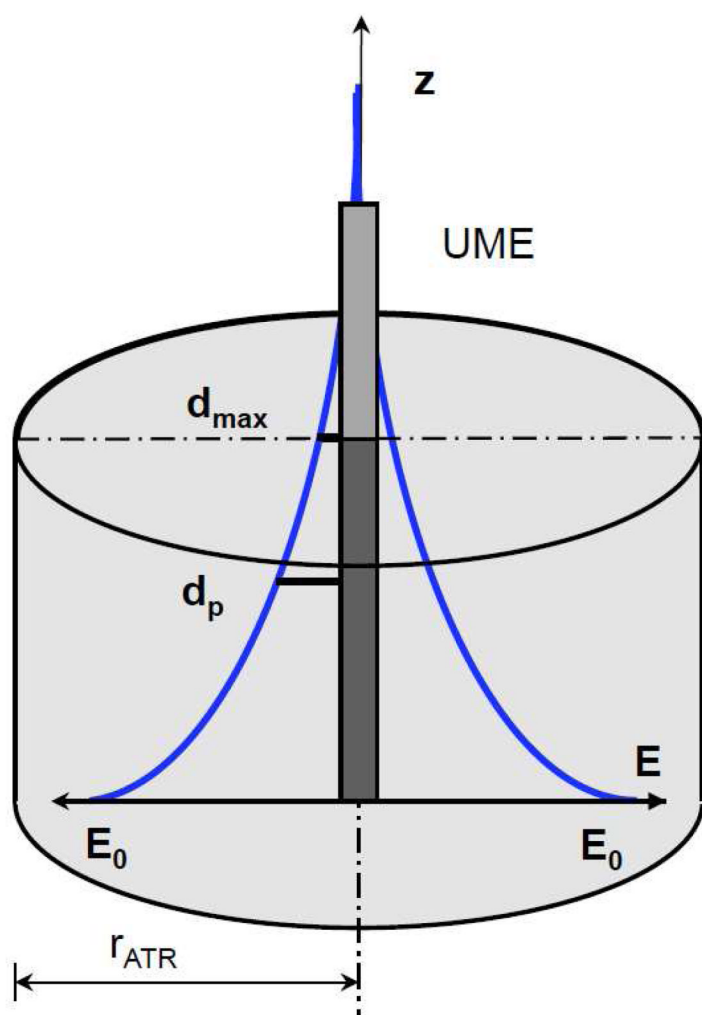
6. Cliffel DE, Bard AJ. *Anal. Chem* 1998;70:1993–1998.
7. Gollas B, Bartlett PN, Denuault G. *Anal. Chem* 2000;72:349–356. [PubMed: 10658330]
8. Hess C, Borgwarth K, Heinze J. *Electrochim. Acta* 2000;45:3725–3736.
9. Gabrielli C, Joiret S, Keddam M, Perrot H, Portail N, Rousseau P, Vivier V. *Electrochim. Acta* 2007;52:7706–7714.
10. Hsu C-Y, Vasantha VS, Ho K-C. *Electrochim. Acta* 2008;53:6244–6251.
11. Williams DE, Mohiuddin TF, Zhu YY. *J. Electrochem. Soc* 1998;145:2664–2672.
12. Treutler TH, Wittstock G. *Electrochim. Acta* 2003;48:2923–2932.
13. Casillas N, James P, Smyrl WH. *J. Electrochem. Soc* 1995;142:L16–L18.
14. Macpherson JV, Unwin PR. *Anal. Chem* 2000;72:276–285. [PubMed: 10658320]
15. Macpherson JV, Unwin PR. *Anal. Chem* 2001;73:550–557. [PubMed: 11217761]
16. Kranz C, Friedbacher G, Mizaikoff B, Lugstein A, Smoliner J, Bertagnolli E. *Anal. Chem* 2001;73:2491–2500. [PubMed: 11403290]
17. Kueng A, Kranz C, Lugstein A, Bertagnolli E, Mizaikoff B. *Angew. Chem. Int. Ed* 2003;42:3238–3240.
18. Davoodi A, Pan J, Leygraf C, Norgren S. *Electrochem. Solid-State Lett* 2005;8:B21–B24.
19. Fasching RJ, Tao Y, Prinz FB. *Sens. Actuators, B* 2005;108:964–972.
20. Gullo MR, Frederix PLTM, Akiyama T, Engel A, de Rooij NF, Staufer U. *Anal. Chem* 2006;78:5436–5442. [PubMed: 16878880]
21. Lee Y, Bard AJ. *Anal. Chem* 2002;74:3626–3633. [PubMed: 12175146]
22. Maruyama K, Ohkawa H, Ogawa S, Ueda A, Niwa O, Suzuki K. *Anal. Chem* 2006;78:1904–1912. [PubMed: 16536427]
23. Evju JK, Smyrl WH. *Proc. Electrochem. Soc* 2001;2001-22:181–192.
24. Evju JK, Smyrl WH. *Proc. Electrochem. Soc* 2002;2000-30:139–154.
25. Boldt F-M, Heinze J, Diez M, Petersen J, Boersch M. *Anal. Chem* 2004;76:3473–3481. [PubMed: 15228313]
26. Fan F-RF, Cliffel D, Bard AJ. *Anal. Chem* 1998;70:2941–2948.
27. Kanoufi F, Cannes C, Zu Y, Bard AJ. *J. Phys. Chem. B* 2001;105:8951–8962.
28. Miao W, Choi J-P, Bard AJ. *J. Am. Chem. Soc* 2002;124:14478–14485. [PubMed: 12452725]
29. Szunerits S, Walt DR. *ChemPhysChem* 2003;4:186–192. [PubMed: 12619418]
30. Szunerits S, Knorr N, Calemczuk R, Livache T. *Langmuir* 2004;20:9236–9241. [PubMed: 15461512]
31. Amphlett JL, Denuault G. *J. Phys. Chem. B* 1998;102:9946–9951.
32. Shao Y, Mirkin MV. *J. Phys. Chem. B* 1998;102:9915–9921.
33. Fulian Q, Fisher AC, Denuault G. *J. Phys. Chem. B* 1999;103:4387–4392.
34. Selzer Y, Mandler D. *Anal. Chem* 2000;72:2383–2390. [PubMed: 10857609]
35. Liljeroth P, Johans C, Slevin CJ, Quinn BM, Kontturi K. *Anal. Chem* 2002;74:1972–1978. [PubMed: 12033294]
36. Sklyar O, Wittstock G. *J. Phys. Chem. B* 2002;106:7499–7508.
37. Sklyar O, Ufheil J, Heinze J, Wittstock G. *Electrochim. Acta* 2003;49:117–128.
38. Zoski CG, Liu B, Bard AJ. *Anal. Chem* 2004;76:3646–3654. [PubMed: 15228336]
39. Combellas C, Fuchs A, Kanoufi F. *Anal. Chem* 2004;76:3612–3618. [PubMed: 15228332]
40. Wipf DO, Bard AJ, Tallman DE. *Anal. Chem* 1993;65:1373–1377.
41. Alpuche-Aviles MA, Wipf DO. *Anal. Chem* 2001;73:4873–4881. [PubMed: 11681463]
42. Ludwig M, Kranz C, Schuhmann W, Gaub HE. *Rev. Sci. Instr* 1995;66:2857–2860.
43. Buchler M, Kelley SC, Smyrl WH. *Electrochem. Solid-State Lett* 2000;3:35–38.
44. Katemann BB, Schulte A, Schuhmann W. *Chem.-Eur. J* 2003;9:2025–2033.
45. Etienne M, Anderson EC, Evans SR, Schuhmann W, Fritsch I. *Anal. Chem* 2006;78:7317–7324. [PubMed: 17037938]
46. Harrick, NJ. *Internal Reflection Spectroscopy*. New York: John Wiley & Sons, Inc; 1967.
47. Hansen DM, Albaugh CE, Moran PD, Kuech TF. *Appl. Phys. Lett* 2001;79:3413–3415.

48. Taft EA. J. Electrochem. Soc 1985;132:2486–2489.

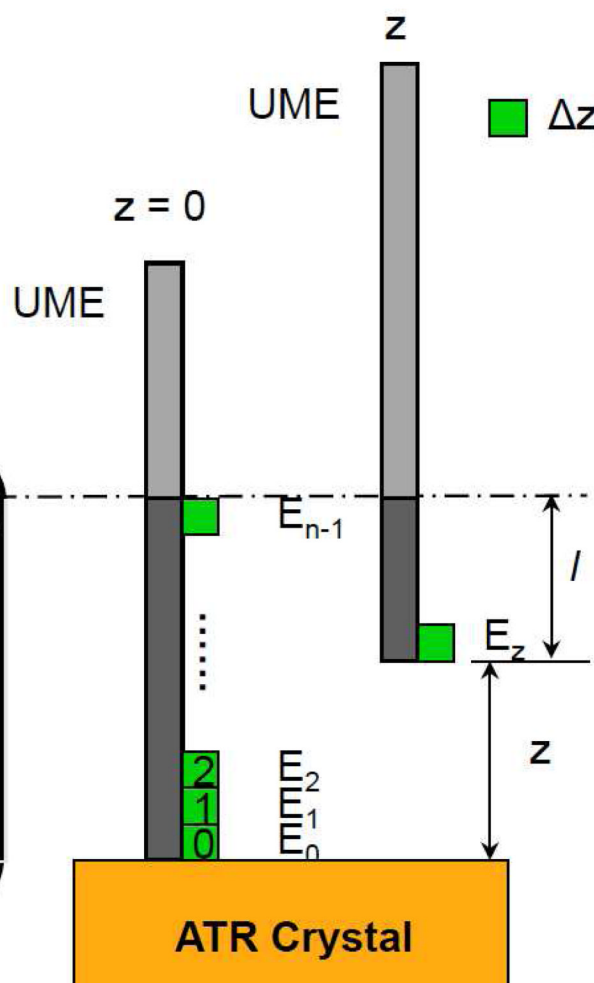


**Figure 1.**  
Schematic view of the IR-ATR-SECM instrument.

a)



b)

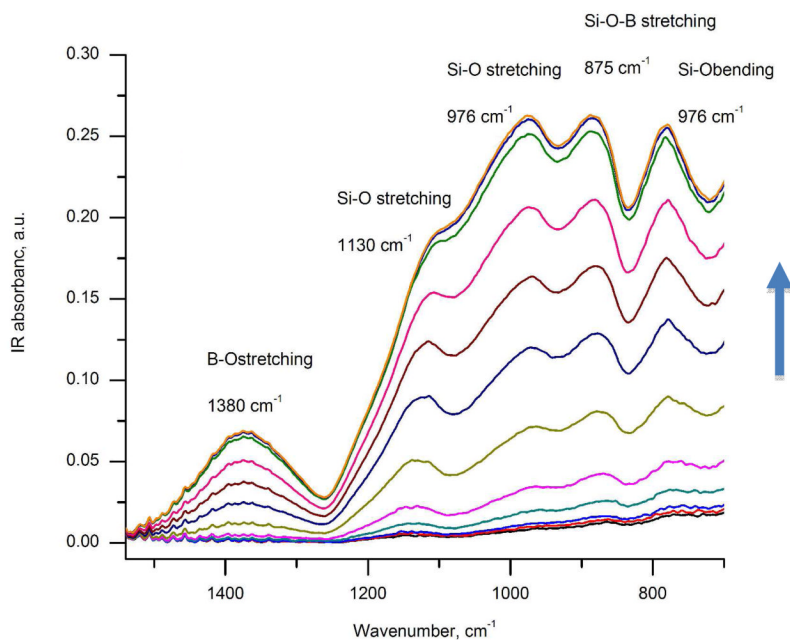
**Figure 2.**

Scheme illustrating the IR signal generation if the UME approaches the IR waveguide surface and penetrates the evanescent field.

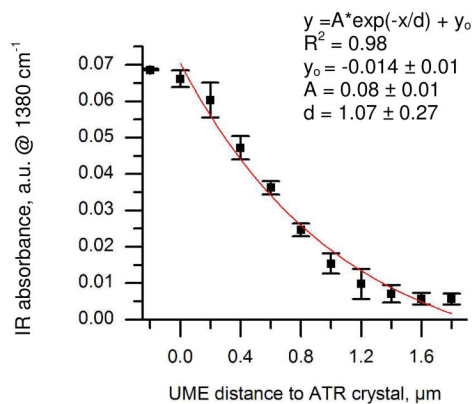
Left: The upper part of the UME colored in light gray presents the part of the UME outside of  $d_{max}$ ; the lower part colored in dark gray represents the part of the UME within  $d_{max}$ ;  $d_p$  is the penetration depth of the evanescent field;  $d_{max}$  is the distance from the ATR crystal surface where no IR absorption from the BSG shielding of the UME is detectable anymore;  $E$  is the intensity of light within the evanescent field;  $E_0$  is the (maximum) intensity of the evanescent field at the surface of the ATR waveguide;  $E_1 - E_{n-1}$  schematically indicate the decreasing intensity of the evanescent field at different positions  $\Delta z$ ,  $z$  is the distance from the ATR crystal surface for an exponentially decayed fraction of the initial energy  $E_0$ ;  $l$  is the fraction of

absorbing material between  $d_{max}$  and  $z$ ;  $r_{ATR}$  is radius of the sensing area of the hemispherical ATR crystal; at  $z = 0$  the UME is touching the ATR crystal surface.

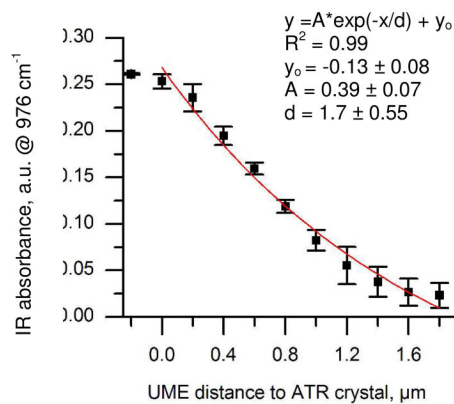
(a)



(b)

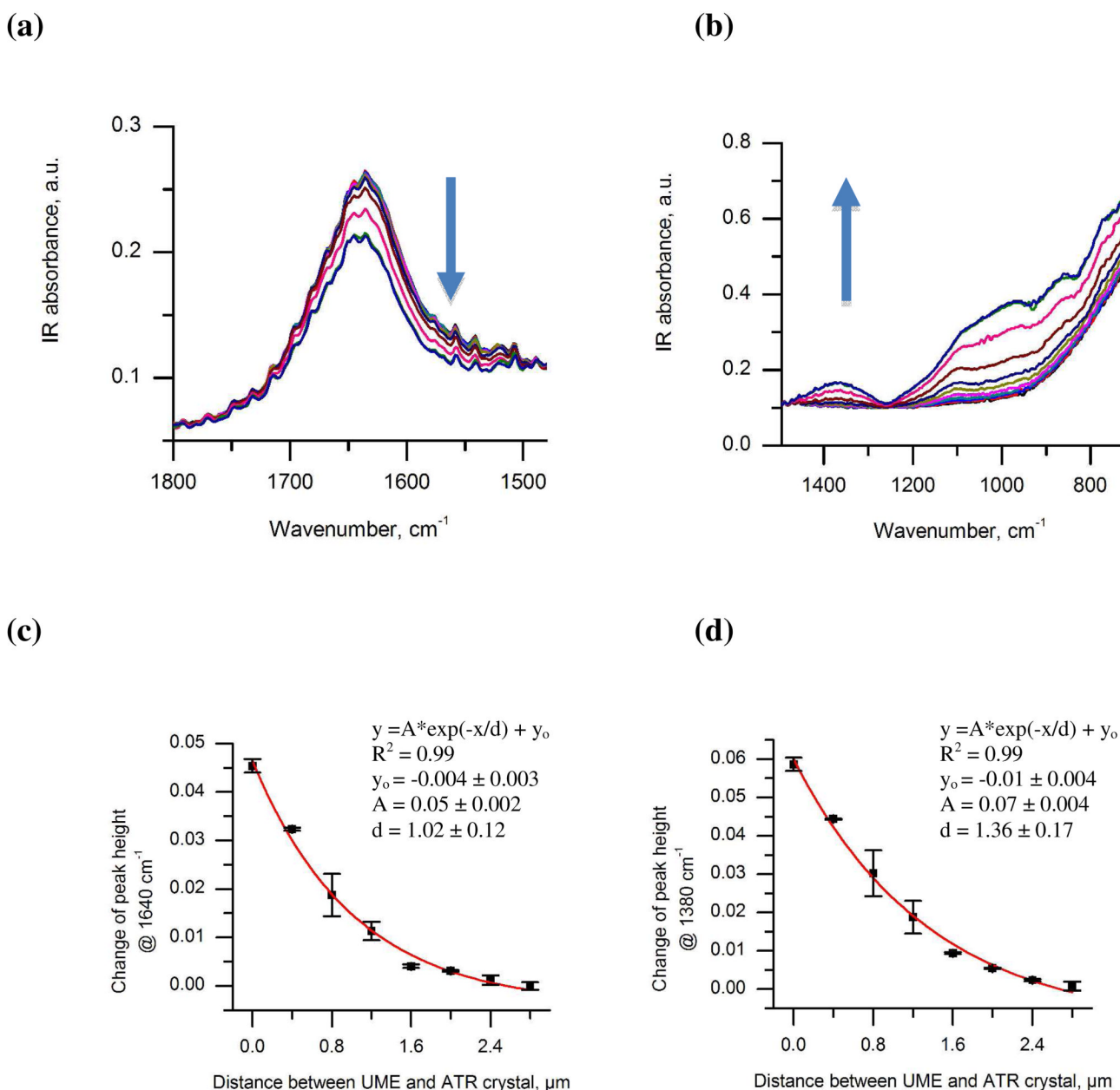


(c)

**Figure 3.**

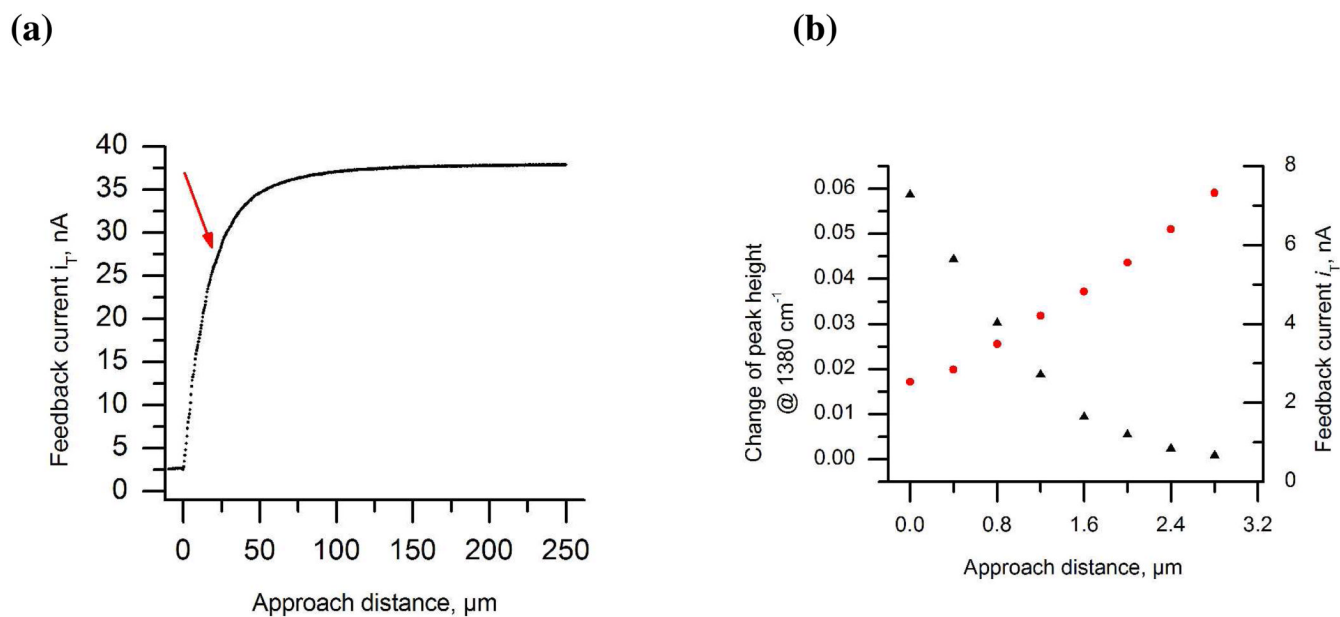
(a) Sequence of IR absorption spectra as the UME approaches the ATR crystal surface in air. IR-ATR approach curves and fitted models for different absorption features are given in (b) for the BSG Bi-O stretching mode at  $1380\text{ cm}^{-1}$ , and in (c) for the BSG Si-O bending mode at  $976\text{ cm}^{-1}$ . The arrow indicates the increase of the BSG absorption features as the UME approaches the ATR waveguide surface. Using equ. 6, the distance to the ATR crystal surface has been modeled (red line).



**Figure 4.**

(a) Sequence of IR absorption spectra as the UME approaches the ATR crystal surface in aqueous 0.02 M  $\text{Ru}(\text{bpy})_3\text{Cl}_2/0.1$  M KCl electrolyte solution showing the decrease of the water O-H bending mode at 1640  $\text{cm}^{-1}$ , while (b) shows the simultaneous increase of BSG absorptions – in particular the Bi-O stretching mode at 1380  $\text{cm}^{-1}$  – when approaching the waveguide surface. (c) IR-ATR approach curve with model fitting evaluating the water O-H bending mode at 1640  $\text{cm}^{-1}$ ; (d) IR-ATR approach curve with fitted model evaluating the BSG Bi-O stretching at 1380  $\text{cm}^{-1}$ . The arrows indicate the decrease of the water absorption feature, and the corresponding increase of the BSG absorption features as the UME approaches the ATR waveguide surface. The overlaid spectra (blue, green) for the water feature – in (a) the lowest two spectra - and the BSG features – in (b) the top two spectra - indicate that the electrode

is touching the ATR crystal surface. Using equ. 6, the distance to the ATR crystal surface has been modeled (red line).

**Figure 5.**

(a) SECM approach curve toward a ZnSe waveguide in 0.02 M  $\text{Ru}(\text{bpy})_3\text{Cl}_2/0.1$  M KCl electrolyte solution. (b) Correlation of SECM and IR-ATR approach curves within 3  $\mu\text{m}$  distance to the ZnSe substrate. Black triangles: IR-ATR data; red dots: feedback mode SECM data.

**Table 1**

Comparison of penetration depths derived from the mathematical model fitted to the experimentally obtained results, and from theoretically calculated values. For these considerations, refractive indices of pure BSG (1.5), and water (1.3) or air (1.0) were used.

	Conditions	$d_p$ @ 1640 cm <sup>-1</sup> [μm]	$d_p$ @ 1380 cm <sup>-1</sup> [μm]	$d_p$ @ 976 cm <sup>-1</sup> [μm]
<b>Mathematical model fitted to experimental data:</b> $d_p = \frac{-z_i}{\ln\left(\frac{Q + A_{IRATR}}{P}\right)}$ (derived from equ. 6)	Approach in air		1.07	1.70
	Approach in H <sub>2</sub> O	1.02	1.36	
<b>Theoretically calculated penetration depth:</b> $d_p = \frac{\lambda}{2\pi\sqrt{n_1^2 \sin^2(\theta) - n_2^2}}$ (equ. 1)	BSG; n <sub>1</sub> =2.4, n <sub>2</sub> =1.5	1.22	1.45	2.05
	H <sub>2</sub> O; n <sub>1</sub> =2.4, n <sub>2</sub> =1.3	0.89	1.06	
	Air; n <sub>1</sub> =2.4, n <sub>2</sub> =1		0.84	1.19